Aalborg Universitet

AALBORG UNIVERSITY
DENMARK

Decoupling Control of Cascaded Power Electronic Transformer based on Feedback Exact Linearization

Sun, Yuwei; Zhu, Jilin; Fu, Chao; Chen, Zhe

Publication date:
2021

Document Version
Accepted author manuscript, peer reviewed version

Link to publication from Aalborg University

IEEE JOURNAL OF EMERGING AND SELECTED TOPICS IN POWER ELECTRONICS

Decoupling Control of Cascaded Power Electronic Transformer based on Feedback Exact Linearization

Yuwei Sun, Jilin Zhu, Chao Fu, and Zhe Chen, Fellow, IEEE

Abstract- **This paper addresses the decoupling control design for the cascaded power electronic transformer (PET) in input-series-output-parallel connection. Due to the coupling and interaction between the sub-modules and between sub-stages, in essence it is a complex nonlinear system. A nonlinear control strategy based on feedback exact linearization (FEL) is developed to decouple all the control objectives so as to realize the dc-link and output voltages fast stabilizing and the submodule balancing without coupling and interactions. Based on the separation of the ac current time-scale and dc voltage time-scale, the FEL control law is derived, and the specific tuning process of control parameters are given for desired control bandwidths. Taken the dynamic influences of the current-loop, filter, and delay into account, further analyses are made and compared with a DAB balancing control-based strategy to show the improvement on decoupling effect and dynamic performance of the proposed control. Finally, the simulation and experimental results verify the theoretical analysis, which exhibit better dynamic features and minimal coupling effect under the condition of bidirectional power changes and parameter inconsistency and uncertainty.**

Index Terms- **Cascaded power electronic transformer; dc-link interaction; balancing control; feedback exact linearization; dual time-scale; decoupling control.**

I. INTRODUCTION

Driven by the demands of intelligence, compatibility, energy saving, environmental protection, and high-power density for electrical equipment in the innovative power systems, the power electronic transformer (PET), also known as the solid-state transformer (SST), has gained extensive attention and developed rapidly. One of the mainstream topologies of PET in high-voltage high-power field is the modular cascaded topology [1-3] which is based on the input-series-output-parallel (ISOP) connection of cascaded H-bridge (CHB) and dual active bridges (DAB).

The cascaded PET possesses many attractive features such as low harmonic, flexible voltage and bidirectional power control, multi-available ac/dc ports, and extendibility with modularization [4, 5], etc. However, higher requirements are

Y. Sun, J. Zhu and C. Fu are with the Department of Electric Power Engineering, North China Electric Power University, Baoding, China (e-mail: sunyuwei@ncepu.edu.cn; zhujilin.1996@qq.com; fuchao@ncepu.edu.cn).
Z. Chen is with the Department of Energy Technology, Aalborg University, Aalborg, Denmark (e-mail: zch@et.aau.dk).

put forward for the control strategies of cascaded PET due to its multistage and modular configuration. To provide excellent interface functions, a fast and accurate regulation of the PET port voltage, current, and bi-directional power in real time should be ensured. Considering the multi-stage conversion interaction and imbalance problem inherent in the modular structure, great efforts should be made for the control of dc-link voltage fast stabilizing and sub-module voltage /current balancing [6,7]. In previous researches on the multi control objectives of cascaded PET, the CHB and DAB stages are usually controlled separately. The grid current and total dc-link voltage are controlled by the dual control loops of CHB converter, while the dc output voltage is regulated by DAB stage. In this control frame, much work on balancing control has been done. A CHB PWM duty-cycle based voltage balancing strategy was proposed in [8]. Due to the limitations of the modulation index, the ability of CHB to deal with unbalanced power is limited, so separate power balance control had to be added to the DAB stage while the DAB currents needed to be measured by more current sensors. Although a current sensor-less power balance control was employed in [9], it still suffered from the complexity of many power sharing controllers. In the methods above, the change of the CHB PWM duty-cycle will lead to the degradation of the ac side current. Therefore, many researchers are inclined to adopt the DAB phase shift modification-based voltage balancing control [10, 11], and the CHB adopts common duty ratio so that the DC-DC stage can be equivalent to an ISOP topology. In this case, the power sharing among modules is naturally attained, so the system complexity can be reduced and the ac side harmonic deterioration can be avoided. For the CHB rectifier, in [12], a control algorithm was proposed to eliminate the coupling effect between the balancing control loops and original system control. Nonetheless, the above researches did not pay much attention to the nonlinearity and coupling between converters, which may deteriorate the dynamic performance and stability under large load step variations common in PET applications.

For the front and rear cascaded system with multi-converters, the load feedforward [13] and positive feedforward [14] methods can be applied to improve the dynamic responses and stability. Similarly, a crossing-feedforward power-voltage sharing controller for the DAB-inverter circuit was proposed in [15], and its stability mechanism based on impedance interaction was explained further in [16]. A linear quadratic regulator was presented to control PET as whole to improve the dynamic performance in [17]. All these methods are instructive to reducing the detrimental interaction and improving dynamics for cascaded converters, although they do not aim at the

modular ISOP-PET and were limited in the analysis from the small signal perspective. Various nonlinear methods have been proved effective in improving the dynamic characteristics and ensuring global stability for the ac-ac SST systems, such as the Lyapunov direct stability control [18], the model predictive control [19], the sliding mode control (SMC) [20], and the feedback linearization-based control [21]. But these studies mainly focused on the rectifier-inverter SST topology based on two-level voltage source converters (VSC), few involved the dynamics and control of multiple DAB modules in a modular SST.

With the development of differential geometry theory, the nonlinear control strategy based on the feedback exact linearization (FEL) becomes an attractive tool for the study of nonlinear systems. One can often find a feedback law to linearize and decouple the multi-input multi-output (MIMO) nonlinear systems, and then a systematic procedure to develop control laws can be provided. It has been widely applied in DC-DC converters [22], three-phase PWM rectifiers [23, 24], active power filters [25], maximum power point tracking of photovoltaic systems [26]. Reference [27] proposed a FEL based nonlinear control for a modular multilevel converter (MMC); Reference [28] presented an application of the FEL technique on the stationary-frame PR grid current control for a CHB rectifier; while References [29] utilize the feedback linearization method for a two-level VSC based AC-AC SST to achieve global asymptotic stability. Both the topologies and control objectives of these references are different compared with the cascaded PET, thus the nonlinear state function models and design process of feedback linearization are different from that of this paper. For the cascaded PET with many H bridges and DABs in ISOP connection in this paper, the nonlinearity not only manifests itself in the variables in one converter, but also exists in the coupling effect between the cascaded stages and modules. Thus, the nonlinear multi-objective decoupling control of cascaded PET using FEL technique needs to be investigated.

The main content of the study can be described as follows:

1) The strategy enables the decoupling linear control design for all the control objectives, including the dc-link and output voltages fast stabilizing and the submodule balancing without coupling and interactions.

2) To simplify the nonlinear control derivations, the FEL strategy are based on two time-scale separation of the PET model. First, the FEL control of the ac current is developed, and then the MIMO affine nonlinear model in the dc voltage time-scale is obtained, and its FEL control law is put forward.

3) Through FEL, all the current and voltage loops can be reduced to a typical second-order system, based on which the desired control bandwidths and damping ratios for the high and low dc bus voltages are easily obtained, irrelevant to outside conditions. This can provide an output features-tailored advantage for the PET in smart grid application.

4) Considering the dynamics of the current loop, control delay, and filter that are ignored in the FEL derivation of the voltage time-scale, further theoretical analysis of the decoupling effect and dynamic performance is made, in

comparison to a previously proposed method. Finally, simulation and experiments provide the validation under bidirectional power variations and parametric uncertainty.

II. MATHEMATICAL MODEL OF CASCADED PET

The topology of the cascaded PET is shown in Fig. 1. It includes a CHB rectifier and N output-parallel DAB modules. L_s is the input inductor; C_1 and C_2 are the dc-link and output capacitors; v_s and i_s are the grid voltage and current; v_{ai} and v_{dci} are the ac and dc-link voltages of CHB, and the subscript $i=1,…,N$, indicating the module numbers; v_o and i_o are the output dc voltage and current. In the specific unit circuit shown in Fig. 1(b), i_{dci} and i_{1i} are the input/output currents of the dc-link capacitors; i_{2i} and i_{oi} are input/output currents of the output capacitors; L_t and n_t are the storage inductance and turns ratio of the high frequency transformer (HFT).
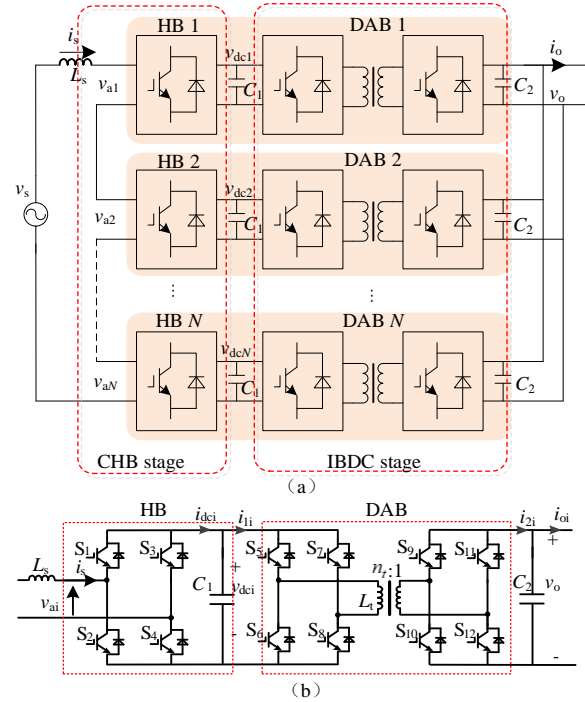

Fig.1 Topology of cascaded PET (a) overall configuration (b) detailed circuit of the sub-module

To simplify the sinusoidal tracking of ac current into a set-point reference regulation problem, the synchronous d-q frame is applied. In order to achieve single-phase d-q transformation, a virtual model orthogonal to the real CHB is built, described as the second equation in (1), while the first is the real one:

$$\begin{cases} \dfrac{di_s}{dt} = -\dfrac{r_s}{L_s}i_s + \dfrac{v_s}{L_s} - \dfrac{1}{L_s}d_s\sum_{i=1}^{N}v_{dci} \\ \dfrac{di_m}{dt} = -\dfrac{r_s}{L_s}i_m + \dfrac{v_m}{L_s} - \dfrac{1}{L_s}d_m\sum_{i=1}^{N}v_{dci} \end{cases} \quad (1)$$

Where, v_m is the virtual grid voltage that lags behind the real voltage v_s by 90°; d_m is the virtual duty cycle that generated by the controller, and i_m is the virtual ac current output by the virtual model [30].

Applying the single-phase d-q transformation [6] to equation (1) yields the current dynamics in the d-q axis:

$$\begin{cases} \dfrac{di_d}{dt} = \dfrac{1}{L_s}(v_d - r_s i_d + \omega L_s i_q - d_d \sum_{i=1}^{N} v_{dci}) \\ \dfrac{di_q}{dt} = \dfrac{1}{L_s}(v_q - r_s i_q - \omega L_s i_d - d_q \sum_{i=1}^{N} v_{dci}) \end{cases} \qquad (2)$$

where v_d, v_q, i_d, i_q, d_d and d_q are respectively the ac voltages, grid currents, and duty ratios in the d-q axis.

For the DAB modeling, applying the single phase-shift control, its average input and output current dynamics under bidirectional power operation are as follows [10]:

$$\begin{cases} i_{1i} = \dfrac{T_{hs} n_t v_o}{L_t} D_i (1 - |D_i|) \\ i_{2i} = \dfrac{T_{hs} n_t v_{dci}}{L_t} D_i (1 - |D_i|) \end{cases}, i = 1, \cdots, N \qquad (3)$$

where, D_i is the phase shift ratio between the primary and secondary sides of DAB and T_{hs} is half of a switching period.

According to Fig.1 and equation (3), the dynamic equations of the dc-link voltages and output voltage of the PET are:

$$\begin{cases} \dfrac{C_1 dv_{dci}}{dt} = i_{dci} - i_{1i} = \dfrac{d_d i_d}{2} - \dfrac{T_{hs} n_t v_o}{L_t} D_i (1 - |D_i|) \\ \dfrac{C_o dv_o}{dt} = \sum_{i=1}^{N} i_{2i} - i_o = \sum_{i=1}^{N} \dfrac{T_{hs} n_t v_{dci}}{L_t} D_i (1 - |D_i|) - i_o \\ i = 1, \cdots, N \end{cases} \qquad (4)$$

where C_o is the equivalent capacitance of the parallel output.

Equations (2) and (4) are the mathematical models that include all the control objectives of cascaded PET, i.e., the d- and q-axis currents i_d and i_q, the N dc-link voltages v_{dc1} - v_{dcN}, and the output voltage v_o. Obviously, the cascaded PET is a complex MIMO nonlinear system, and the nonlinearity not only exists within one sub-converter, but also presents at the inter-module and sub-stage interactions. By observing (2) and (4), if perform the FEL technique on the model directly, there will be one zero-dynamic state left since the number of control inputs (including d_d, d_q, D_1-D_N) is one less than that of the control objectives.

As discussed in [24], for exact linearization of the PWM rectifier, when taking i_d and i_q as the outputs, the dc-voltage will be the zero-dynamics. It is suggested to be controlled by a PI controller cascaded to the i_d loop, which is nothing but an outer-voltage loop in view of the configuration. In this paper, to avoid the zero-dynamics analysis and considering the much larger ac current control bandwidth than the dc voltage control bandwidth, the FEL process are deduced on two time-scale separation. The currents are first controlled by FEL in a faster time-scale, on this basis the output and dc-link voltages can be exactly linearized and controlled in a slower time-scale. The desired control bandwidths of different time-scale loops can be obtained based on the simplified linear models.

III. NONLINEAR DECOUPLING CONTROL OF CASCADED PET

In this section, brief review of the FEL control theory is presented and then it is applied to the current time-scale and voltage time-scale control of the cascaded PET, respectively.

A. Feedback Exact Linearization for MIMO System

The FEL control theory is briefly described as follows [31]. Consider the following MIMO nonlinear system

$$\begin{cases} \dot{x} = f(x) + g(x)u \\ y = h(x) \end{cases} \qquad (5)$$

where, x is the state vector; u is the control inputs and y is the outputs, note that it is a square system with the same number m of inputs and outputs; f and g are the smooth vector fields and h is a smooth scalar function vector.

According to [31], the multivariable nonlinear system of the form (5) has a relative degree $\{r_1, r_2 \dots r_m\}$ at x^0 if:

(i) $$L_{g_j} L_f^k h_i(x) = 0 \qquad (6)$$

for all $1 \le j \le m$, for all $k < r_i - 1$, for all $1 \le i \le m$, and for all x in a neighborhood of x^0,

(ii) the $m \times m$ matrix

$$E(x) = \begin{bmatrix} L_{g_1} L_f^{r_1-1} h_1(x) & L_{g_2} L_f^{r_1-1} h_1(x) & \cdots & L_{g_m} L_f^{r_1-1} h_1(x) \\ L_{g_1} L_f^{r_2-1} h_2(x) & L_{g_2} L_f^{r_2-1} h_2(x) & \cdots & L_{g_m} L_f^{r_2-1} h_2(x) \\ \vdots & \vdots & \cdots & \vdots \\ L_{g_1} L_f^{r_m-1} h_m(x) & L_{g_2} L_f^{r_m-1} h_m(x) & \cdots & L_{g_m} L_f^{r_m-1} h_m(x) \end{bmatrix} \qquad (7)$$

is nonsingular at x^0, where $L_f h$ and $L_g h$ represent the Lie derivatives of $h(x)$ along $f(x)$ and $g(x)$, respectively.

For a nonlinear system (5) with well-defined relative degree $\{r_1, r_2 \dots r_m\}$ at x^0 and that $r_1 + r_2 + \cdots r_m = n$ (n is the state vector dimension), the local coordinate transform and a state feedback exist, with the form of (8) and (9) respectively.

$$z = \phi(x) = \begin{bmatrix} z_1 \\ z_2 \\ \vdots \\ z_m \end{bmatrix}, \quad z_i = \begin{bmatrix} L_f^0 h_i(x) \\ L_f^1 h_i(x) \\ \vdots \\ L_f^{r_i-1} h_i(x) \end{bmatrix}, \text{ for } 1 \le i \le m \quad (8)$$

$$u = -E^{-1}(x)a(x) + E^{-1}(x)v \qquad (9)$$

where $a(x) = \begin{bmatrix} L_f^{r_1} h_1(x) & L_f^{r_2} h_2(x) & \cdots & L_f^{r_m} h_m(x) \end{bmatrix}^T$, and $v = \begin{bmatrix} v_1 & \cdots & v_m \end{bmatrix}^T$ is the new control input vector.

In the new coordinates and with state feedback, the original system (5) can be linearized as Brunovsky canonical form

$$\begin{cases} \dot{z} = Az + Bv \\ A = \text{diag}[A_1, \cdots, A_m], \quad B = \text{diag}[b_1, \cdots, b_m] \end{cases} \qquad (10)$$

where A_i is the $r_i \times r_i$ matrix,

$$A_i = \begin{bmatrix} 0 & 1 & \cdots & 0 \\ \vdots & \ddots & \ddots & \vdots \\ 0 & \cdots & \ddots & 1 \\ 0 & \cdots & \cdots & 0 \end{bmatrix},$$

and b_i is the $r_i \times 1$ vector $b_i = \begin{bmatrix} 0 & \cdots & 0 & 1 \end{bmatrix}^T$.

Note that (8)-(10) are the general FEL results for a MIMO nonlinear system with relative degree $\{r_1, \dots, r_m\}$. In a particular case when $r_1 = \dots = r_m = 1$, z_i will be scalar function $h_i(x)$, $b_i = 1$, A will be a zero matrix, and B is a $m \times m$ unit matrix, then the

Brunovsky form (10) will be simplified as $\dot{z} = v$.

B. Grid Current Control Law

The grid current control is designed based on applying the feedback compensation to the subsystem equation (2). By selecting the state variables as $x_I = [i_d \; i_q]$, the control inputs as $u_I = [d_d \; d_q]$, the outputs as $y_I = [i_d - i_{dref} \; i_q - i_{qref}]$ and following the exact linearizing procedure described in Part A, the feedback control law can be derived as in (11), which transform the original system (2) into a linear one (12).

$$\begin{bmatrix} d_d \\ d_q \end{bmatrix} = \frac{1}{\sum_{i=1}^{N} v_{dci}} \begin{bmatrix} v_d - r_s i_d + \omega L_s i_q - L_s v_{I1} \\ v_q - r_s i_q - \omega L_s i_d - L_s v_{I2} \end{bmatrix} \quad (11)$$

$$\begin{bmatrix} \dot{i}_d \\ \dot{i}_q \end{bmatrix} = \begin{bmatrix} v_{I1} \\ v_{I2} \end{bmatrix} \quad (12)$$

In (12), the new input vector $v_I = [v_{I1} \; v_{I2}]^T$ can be obtained by applying a PI controller, i.e.,

$$\begin{bmatrix} v_{I1} \\ v_{I2} \end{bmatrix} = \begin{bmatrix} k_{Ip}(i_{dref} - i_d) + k_{Ii} \int (i_{dref} - i_d) \, dt \\ k_{Ip}(i_{qref} - i_q) + k_{Ii} \int (i_{qref} - i_q) \, dt \end{bmatrix} \quad (13)$$

The proportional and integral gains, k_{Ip}, k_{Ii}, will be selected in part D, section III according to the classical linear control theory. As a result, the grid current control diagram of PET is shown in Fig. 2, which essentially is a synchronous d-q frame PI decoupling control from the control structure point of view. As it is directly resulted from exact linearization of the current model, it features global validity of the designed performance, and reduced difficulty in controller parameter design.
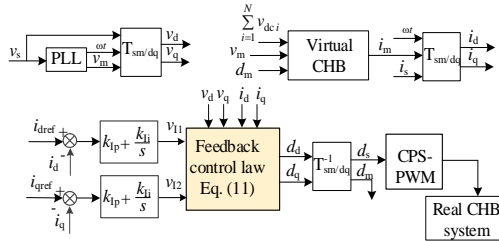

Fig.2 Block diagram of grid current control loop

C. Dc-link and Output Voltages Control Law

For the control of the voltage time-scale, there are N dc-link voltages v_{dc1}-v_{dcN} and one output voltage v_o need to be controlled. To reduce the design complexity of the voltage control law, the ac current loop dynamics is reduced into a unit transfer function here since the time-scale separation. The feasibility of this approximation will be proved by the step responses comparison between the simplified model and the detailed switching circuit, given in part D.

According to active power conservation, the following equation is deduced.

$$\begin{cases} P_{ac} = \dfrac{v_d i_d}{2} = \sum_{i=1}^{N} v_{dci} i_{dc} \\ i_{dc} = \dfrac{v_d i_d}{2 \sum_{i=1}^{N} v_{dci}} = \dfrac{v_d}{2 \sum_{i=1}^{N} v_{dci}} i_{dref} \end{cases} \quad (14)$$

where P_{ac} is the active power of the PET ac side.

Substituting (14) in to (4), the dynamic models of the N dc-link voltages and one output voltage can be expressed as

$$\begin{cases} \dfrac{dv_{dc1}}{dt} = -\dfrac{T_{hs} n_t v_o}{C_1 L_t} D_1(1 - |D_1|) + \dfrac{v_d}{2C_1 \sum_{i=1}^{N} v_{dci}} i_{dref} \\ \quad \vdots \\ \dfrac{dv_{dcN}}{dt} = -\dfrac{T_{hs} n_t v_o}{C_1 L_t} D_N(1 - |D_N|) + \dfrac{v_d}{2C_1 \sum_{i=1}^{N} v_{dci}} i_{dref} \\ \dfrac{dv_o}{dt} = \dfrac{1}{C_o} \sum_{i=1}^{N} \dfrac{T_{hs} n_t v_{dci}}{L_t} D_i(1 - |D_i|) - \dfrac{1}{C_o} i_o \end{cases} \quad (15)$$

Defining the state vector as $x = [v_{dc1} \; v_{dc2} \; \dots \; v_{dcN} \; v_o]^T$, when expressing the above model in the affine nonlinear MIMO form of (5), we obtain

$$f(x) = \begin{bmatrix} 0 & \dots & 0 & -\dfrac{i_o}{C_o} \end{bmatrix}^T \quad (16)$$

$$g(x) = \begin{pmatrix} g_{1,1} & 0 & \cdots & 0 & g_{N+1,1} \\ 0 & g_{2,2} & \cdots & 0 & g_{N+1,2} \\ \vdots & 0 & \cdots & \vdots & \vdots \\ 0 & \vdots & \cdots & g_{N,N} & g_{N+1,N} \\ g_{1,N+1} & g_{2,N+1} & \cdots & g_{N,N+1} & 0 \end{pmatrix} \quad (17a)$$

$$g_{1,1} = g_{2,2} = \cdots = g_{i,i} = \cdots g_{N,N} = -T_{hs} n_t v_o / (C_1 L_t)$$
$$\quad (17b)$$
$$g_{i,N+1} = \frac{T_{hs} n_t v_{dci}}{C_o L_t}, \; g_{N+1,i} = v_d / (2C_1 \sum_{i=1}^{N} v_{dci})$$

$$u = \begin{bmatrix} u_1 \\ \vdots \\ u_N \\ u_{N+1} \end{bmatrix} = \begin{bmatrix} M_1 \\ \vdots \\ M_N \\ i_{dref} \end{bmatrix} = \begin{bmatrix} D_1(1 - |D_1|) \\ \vdots \\ D_N(1 - |D_N|) \\ i_{dref} \end{bmatrix} \quad (18)$$

$$\begin{cases} y_1 = h_1(x) = v_{dc1} - v_{dcref} \\ \quad \vdots \\ y_N = h_N(x) = v_{dcN} - v_{dcref} \\ y_{N+1} = h_{N+1}(x) = v_o - v_{oref} \end{cases} \quad (19)$$

In (18), the variables, $M_i = D_i(1 - |D_i|)$, are regarded as the control inputs of the DABs for convenience. After M_i is obtained, the phase shift ratio D_i can easily be determined by a lookup table. The active current reference i_{dref} is also regarded as one control input, so system (15) becomes an $N+1$ dimensional square system.

Then following the FEL procedure described in Part A, the feedback control law of system (15) can be obtained:

$$u = -E^{-1}(x)a(x) + E^{-1}(x)v$$

$$
\begin{bmatrix} u_1 \\ u_2 \\ \vdots \\ u_N \\ i_{dref} \end{bmatrix} = \begin{bmatrix} k_A v_1 + k_B i_{dref} \\ k_A v_2 + k_B i_{dref} \\ \vdots \\ k_A v_N + k_B i_{dref} \\ k_C \sum_{i=1}^{N} v_{dci} v_i + k_D (v_{N+1} + \dfrac{i_o}{C_o}) \end{bmatrix}
\tag{20}
$$

where, $f_{Ti} = T_{hs} n_t / L_t$;

$$k_A = \frac{-C_1}{f_{Ti} v_o}, k_B = \frac{v_d}{2 \sum v_{dci} f_{Ti} v_o}, k_C = \frac{2C_1}{v_d}, k_D = \frac{2C_o v_o}{v_d}.$$

By (20), the original nonlinear system (15)-(19) can be transformed into the simple first-order differential linear form.

$$
\begin{bmatrix} \dot{v}_{dc1} \\ \vdots \\ \dot{v}_{dcN} \\ \dot{v}_o \end{bmatrix} = \begin{bmatrix} v_1 \\ \vdots \\ v_N \\ v_{N+1} \end{bmatrix}
\tag{21}
$$

A PI controller is used to give the new control variables v_i:

$$
\begin{bmatrix} v_1 \\ \vdots \\ v_N \\ v_{N+1} \end{bmatrix} = \begin{bmatrix} k_{vp}(v_{dcref} - v_{dc1}) + k_{vi}\int (v_{dcref} - v_{dc1})dt \\ \vdots \\ k_{vp}(v_{dcref} - v_{dcN}) + k_{vi}\int (v_{dcref} - v_{dcN})dt \\ k_{vp}(v_{oref} - v_o) + k_{vi}\int (v_{oref} - v_o)dt \end{bmatrix}
\tag{22}
$$

where, k_{vp} and k_{vi} are the proportional and integral gains.

The overall control diagram of cascaded PET is illustrated in Fig. 3, where G_d and G_o denotes the PI controllers in (22). The function f^{-1} represents the calculation process from M_i to D_i. It is apparent that the dc link voltages will be balanced when they track the same reference, consequently the output currents can be shared due to the ISOP structure [10,11].
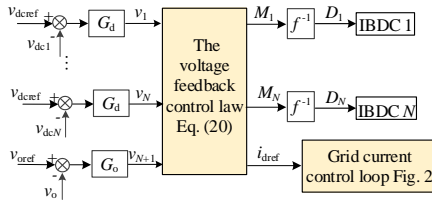

Fig.3 Block diagram of voltage loop control of PET

D. Control Parameter Design for the Dual Time-Scale Loops

After applying the FEL technique on the current and voltage time-scale control separately, the multi control objectives are linearized and decoupled to which regular linear designs can be used. As can be derived from (12)-(13) and (21)-(22), both the ac current and dc voltages control can be presented as a common second-order linear control loop form, as shown in Fig. 4. The closed loop transfer function is in (23).
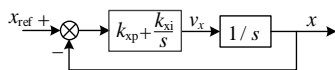

Fig.4 Common second-order linear form of the multiple control loops

$$T_x(s) = \frac{x}{x_{ref}} = \frac{k_{xp}s + k_{xi}}{s^2 + k_{xp}s + k_{xi}}
\tag{23}$$

where, x represents any of the controlled variables, including i_d, i_q, v_{dci} and v_o; x_{ref} represents their references, i.e., i_{dref}, i_{qref}, v_{dcref} and v_{oref}; k_{xp} and k_{xi} are the corresponding proportional and integral gains.

Expressing equation (23) as the typical second-order system,

$$T_x(s) = \frac{2\xi_x \omega_{nx} s + \omega_{nx}^2}{s^2 + 2\xi_x \omega_{nx} s + \omega_{nx}^2}
\tag{24}$$

where ξ_x is the damping ratio and ω_{nx} is the natural angular frequency. According to the definition of control bandwidth, we can obtain:

$$
\begin{cases} k_{xp} = 2\xi_x \omega_{nx} = \dfrac{2\xi_x \omega_{bx}}{\sqrt{(1+2\xi_x^2) + \sqrt{(1+2\xi_x^2)^2 + 1}}} \\[2mm] k_{xi} = \omega_{nx}^2 = \dfrac{\omega_{bx}^2}{(1+2\xi_x^2) + \sqrt{(1+2\xi_x^2)^2 + 1}} \end{cases}
\tag{25}
$$

where f_{bx} is the control bandwidth and $\omega_{bx}=2\pi f_{bx}$.

From (25), the PI parameters can be calculated by selecting desired control bandwidths and damping ratios of the different control objectives. Based on the optimal control principle of second-order system, the damping ratio ξ_x can be selected as 0.707. When specifying the control bandwidths, the following criterions need to be considered. One is that different time-scales, including the PWM switching time-scale, current control time-scale and dc voltage control time-scale, should be separated; the second is that preferable dynamic responses must be ensured for all the variables. Therefore, an order of magnitude difference in bandwidth can be selected:

$$f_{sw} \approx 10^1 f_{bI} \approx 10^2 f_{bV}
\tag{26}$$

where f_{sw} is the PWM frequency, f_{bI} and f_{bV} are the control bandwidths of grid current loop and voltage loop, respectively. For example, when f_{bI}=370Hz, about 1/10 of the equivalent switching frequency of the HB rectifier, the parameters of the current loop are calculated as k_{Ip}=1600 and k_{Ii}=1.28×10⁶. By reducing a time-scale, f_{bV}=37Hz, and the voltage loop gains k_{vp}=160 and k_{vi}=12800. Finally, the Bode plots with these PI parameters are given in Fig. 5, where the control bandwidths are consistent with the above ones and a phase margin of 65.4° can be read in both loops.
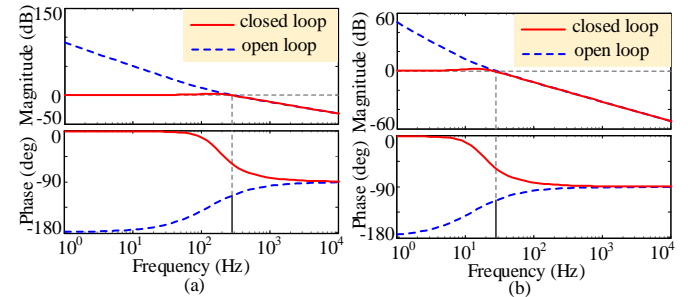

Fig.5 Bode plots of the dual time-scale control loops (a) grid current control (b) dc-links /output voltage control

To verify the effectiveness of the simplified second-order linear model described in (23), the step responses are also given

and compared with a detailed switching circuit in MATLAB /Simulink. As can be seen in Fig. 6, the curves show high degree of similarity. Therefore, the feasibility of ignoring the dynamic process of the current loop in the voltage modelling and control can be proved.
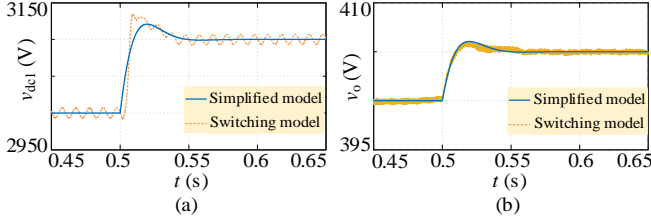

Fig.6 Step response comparison between simplified model and detailed switching model (a) dc-link voltage (b) output voltage

Another concern about the model accuracy is the effect of the control delay with using the digital control. Generally, when the current loop bandwidth is far below the control frequency and the switching frequency (limited by the design criterion (26)), it is not hard to prove that the control delay has little effect on the frequency range (medium and low frequency) that we focus on. Adopting the simplified model to design the controller is still feasible.

E. Double Line-Frequency Ripple Suppression

For the cascaded PET, there inherently exist the second-order ripple voltages in the dc-link which is undesired to be coupled to the ac current control loop and DAB stage. The performance of the second-order harmonic suppression of the proposed control should be discussed.

The steady-state dc-link voltages can be expressed as the summation of the dc and ripple components

$$v_{dci} = v_{dcref} + \tilde{v}_{dc} \tag{27}$$

where $\tilde{v}_{dc}$ is the second-order ripple voltage.

Substituting (22) and (27) into (20), the control input variables of the CHB and DAB circuits can be expressed as

$$
\begin{aligned}
i_{dref} &= k_C \sum_{i=1}^{N} v_{dci} v_i + k_D (v_{N+1} + \frac{i_o}{C_o}) \\
&= -\frac{2C_1 G_d N}{v_d} v_{dcref} \tilde{v}_{dc} + \frac{2C_o v_o}{v_d}(G_o(v_{oref} - v_o) + \frac{i_o}{C_o})
\end{aligned} \tag{28}
$$

$$
\begin{aligned}
M_i &= k_A v_i + k_B i_{dref} \\
&= [C_o G_o (v_{oref} - v_o) + i_o] / (f_{Ti} N v_{dcref})
\end{aligned} \tag{29}
$$

where G_d and G_o are the transfer functions of the PI controllers, as shown in Fig. 3.

According to (29), one can see that the phase shift function of DAB, M_i, does not contain the ripple voltage term $\tilde{v}_{dc}$, which means the second-order ripples will not be transferred to the DAB stage by the nonlinear control. However, from (28), as the ripple voltage is contained in the d-axis current reference i_{dref}, it will cause odd harmonics of the grid current. Thereby a second-order notch filter is added to i_{dref} before it passing on to the current loop, as shown in Fig. 7(a).

$$G_{notch}(s) = \frac{i'_{dref}}{i_{dref}} = \frac{s^2 + \omega_n^2}{s^2 + (\omega_n / Q)s + \omega_n^2} \tag{30}$$

where, Q is the quality factor of the notch filters and ω_n is the natural frequency.

## IV. DYNAMIC PERFORMANCE AND DECOUPLING EFFECT ANALYSIS

As known from the numerous researches on the power electronic systems, the coupling (or interaction) effects in the circuit will deteriorate the dynamic performance of the control loops. In this section, analytical evaluation of the dynamic and decoupling performance will be presented from the perspective of the dc-link voltages and output voltage control.

From the linearized equations (21) and (22), the ideal state-space equation under the proposed control can be expressed as

$$
\begin{bmatrix} sv_{dc1} \\ \vdots \\ sv_{dcN} \\ sv_o \end{bmatrix} = -\begin{bmatrix} G_d & 0 & \cdots & 0 \\ 0 & \ddots & \ddots & \vdots \\ \vdots & \ddots & G_d & 0 \\ 0 & \cdots & 0 & G_o \end{bmatrix}\begin{bmatrix} v_{dc1} \\ \vdots \\ v_{dcN} \\ v_o \end{bmatrix} \tag{31}
$$

It can be observed that all the controlled objectives, including v_{dc1}-v_{dcN} and v_o, are decoupled by using the FEL technique theoretically. Unfortunately, there are some factors that are not included in (31) and needed to consider further, such as the current loop dynamics which is ignored in derivation of the voltage control law, and the notch filter which is added for suppressing the second-order ripples. In the following, the impact of the dynamics of the current loop, filter, and control delay on the decoupling effect will be analyzed, and the comparison between a previously proposed control strategy will be made.

For the convenience of comparison analysis, the proposed control strategy is rearranged into the diagram of Fig. 7(a), referred to as Control strategy I. While in Fig. 7(b), the DAB-balancing control-based strategy is chosen for comparison, considering of its good performance and simplicity [10,11], referred to as Control strategy II. In Fig. 7(b), the dc-link voltages are balanced by the DABs, while the CHB adopts a common duty ratio so that the output-parallel DABs can be equivalent to an ISOP structure; in such way the output current sharing can be naturally attained.
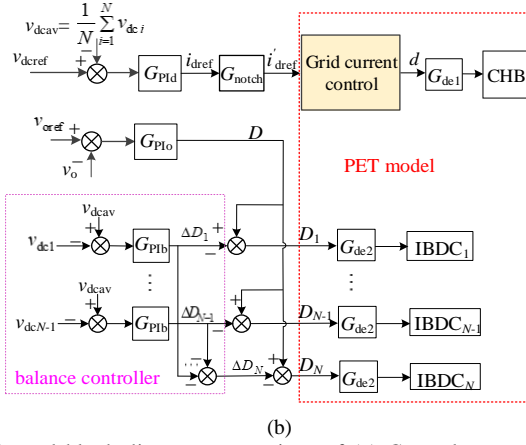

(a)

(b)
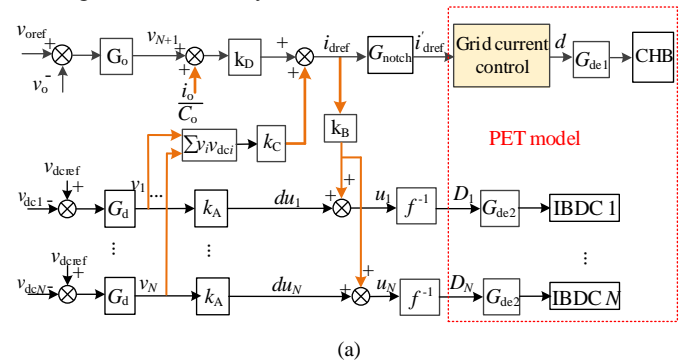
Fig.7 Control block diagram comparison of (a) Control strategy I (the proposed control) and (b) Control strategy II (the strategy based on DAB-balancing control)

For better comparison, the same grid-current controller (Fig. 2) and notch filter (equation (30)) are employed for Control strategy II. Thus, the two strategies have a same dynamic process of the grid current loop:

$$G_{is} = \frac{i_d}{i'_{dref}} = \frac{(sk_{Ip} + k_{Ii})G_{de1}}{s^2 + (sk_{Ip} + k_{Ii})G_{de1}} \quad (32)$$

where the CHB control delay $G_{de1} = 1/(T_c s + 1)$. T_c is the total delay time including one computation period and one PWM delay which is 0.25 times of the switching period.

Taking the influences of the omitted current loop dynamics and control delay, the nonlinear model of PET in the voltage time-scale (equation (15)) can be rewritten as follows:

$$\begin{cases} sv_{dc1} = -f_{Ti}\dfrac{v_o}{C_1}G_{de2}D_1(1-|D_1|) + \dfrac{v_d G_{is}i'_{dref}}{2C_1\sum_{i=1}^{N}v_{dci}} \\ \vdots \\ sv_{dcN} = -f_{Ti}\dfrac{v_o}{C_1}G_{de2}D_N(1-|D_N|) + \dfrac{v_d G_{is}i'_{dref}}{2C_1\sum_{i=1}^{N}v_{dci}} \\ sv_o = \dfrac{1}{C_o}\sum_{i=1}^{N}f_{Ti}v_{dci}G_{de2}D_i(1-|D_i|) - \dfrac{1}{C_o}i_o \end{cases} \quad (33)$$

where the control delay $G_{de2} = 1/(T_d s + 1)$. T_d is the total delay time of DAB, which includes one computation period and one PWM delay that equals 0.25 times of the switching period.

A. Decoupling Effect between the Multi-Control Loops
1) Control strategy I

From Fig. 7(a), the control variables $u_i = M_i = D_i(1-|D_i|)$ $(i=1,…,N)$ and i'_{dref} can be calculated as:

$$\begin{cases} i'_{dref} = \dfrac{2G_{notch}}{v_d}[(G_oC_o(v_{oref} - v_o) + i_o)v_o + C_1G_d\sum v_{dci}(v_{dcref} - v_{dci})] \\ M_i = \dfrac{G_oC_o(v_{oref} - v_o) + i_o}{f_{Ti}\sum v_{dci}} + \dfrac{C_1G_d}{f_{Ti}v_o}[\dfrac{\sum(v_{dcref} - v_{dci})}{N} - (v_{dcref} - v_{dci})] \end{cases} \quad (34)$$

Substituting (34) into the system equation (33) and not considering the changes of the reference voltages yields the small signal state-space equation:

$$\begin{bmatrix} s\hat{v}_{dc1} \\ \vdots \\ s\hat{v}_{dcN} \\ s\hat{v}_o \end{bmatrix} = A\begin{bmatrix} \hat{v}_{dc1} \\ \vdots \\ \hat{v}_{dcN} \\ \hat{v}_o \end{bmatrix} + B\hat{i}_o \quad (35)$$

$$\begin{cases} A = \begin{bmatrix} a_{1,1} & \cdots & a_{1,N} & a_{1,N+1} \\ \vdots & \ddots & \vdots & \vdots \\ a_{N,1} & \cdots & a_{N,N} & a_{N,N+1} \\ 0 & \cdots & 0 & a_{N+1,N+1} \end{bmatrix} \\ B = \begin{bmatrix} b_1 & \cdots & b_N & b_{N+1} \end{bmatrix}^T \end{cases} \quad (36)$$

where

$$\begin{cases} a_{i,i(i=1\sim N)} = -\dfrac{G_d}{N}[G_{notch}G_{is} + (N-1)G_{de2}] \\ a_{N+1,N+1} = -G_{de2}G_o \\ a_{i,j(i,j=1\sim N,i\neq j)} = -\dfrac{G_d}{N}(G_{notch}G_{is} - G_{de2}) \\ a_{i,N+1(i=1\sim N)} = (Nf_{Ti}Mv_{dcref} - G_oC_ov_{oref})\dfrac{(G_{notch}G_{is} - G_{de2})}{C_1Nv_{dcref}} \\ b_{i(i=1\sim N)} = v_{oref}\dfrac{(G_{notch}G_{is} - G_{de2})}{C_1Nv_{dcref}} \\ b_{N+1} = (G_{de2} - 1)/C_o \end{cases} \quad (37)$$

where M is the steady state value of M_i.

As shown in (35)-(37), there are nonzero off-diagonal elements in the state matrix A, which means that the dynamics of the dc-link voltage and output voltage loops are mutually influenced. The transfer function from the output voltage to the dc-link voltage can be deduced as in (38) (the process is given in the appendix):

$$\dfrac{\hat{v}_{dci}}{\hat{v}_o} = \dfrac{G_{is}G_{notch} - G_{de2}}{sC_1 + G_dC_1G_{is}G_{notch}}(f_{Ti}M - \dfrac{G_oC_ov_{oref}}{Nv_{dcref}}) \quad (38)$$

2) Control strategy II

Based on the PET model (equation (33)) and Fig. 7(b), the small signal state-space equation under Control strategy II can be deduced as follows: (the process is given in the appendix):

$$\begin{bmatrix} s\hat{v}_{dc1} \\ \vdots \\ s\hat{v}_{dcN} \\ s\hat{v}_o \end{bmatrix} = A'\begin{bmatrix} \hat{v}_{dc1} \\ \vdots \\ \hat{v}_{dcN} \\ \hat{v}_o \end{bmatrix} + B'\hat{i}_o \quad (39)$$

$$\begin{cases} A' = \begin{bmatrix} a'_{1,1} & \cdots & a'_{1,N} & a'_{1,N+1} \\ \vdots & \ddots & \vdots & \vdots \\ a'_{N,1} & \cdots & a'_{N,N} & a'_{N,N+1} \\ a'_{N+1,1} & \cdots & a'_{N+1,N} & a'_{N+1,N+1} \end{bmatrix} \\ B' = \begin{bmatrix} 0 & \cdots & 0 & -1/C_o \end{bmatrix}^T \end{cases} \quad (40)$$

where

$$\begin{cases} a'_{i,i(i=1\sim N)} = \dfrac{(1-N)f_{\mathrm{Ti}}G_{\mathrm{de2}}v_{\mathrm{oref}}(1-2|D|)G_{\mathrm{PIb}} - d_{\mathrm{d}}^*G_{\mathrm{is}}G_{\mathrm{PId}}G_{\mathrm{notch}}}{NC_1} \\[2mm] a'_{N+1,N+1} = \dfrac{-f_{\mathrm{Ti}}G_{\mathrm{de2}}Nv_{\mathrm{dcref}}(1-2|D|)G_{\mathrm{PIo}}}{C_o} \\[2mm] a'_{i,j(i,j=1\sim N,i\ne j)} = \dfrac{-d_{\mathrm{d}}^*G_{\mathrm{is}}G_{\mathrm{PId}}G_{\mathrm{notch}} + f_{\mathrm{Ti}}G_{\mathrm{de2}}v_{\mathrm{oref}}(1-2|D|)G_{\mathrm{PIb}}}{NC_1} \\[2mm] a'_{i,N+1(i=1\sim N)} = \dfrac{f_{\mathrm{Ti}}G_{\mathrm{de2}}[v_{\mathrm{oref}}(1-2|D|)G_{\mathrm{PIo}} - D(1-|D|)]}{C_1} \\[2mm] a'_{N+1,j(j=1\sim N)} = \dfrac{f_{\mathrm{Ti}}G_{\mathrm{de2}}D(1-|D|)}{C_o} \end{cases}$$
(41)

Obviously, the matrix A' is off-diagonal, so that each of the dc-link voltages and the output voltage are coupled in dynamic states. To show the coupling intensity, the transfer function from the output voltage to the dc-link voltage under Control strategy II is obtained (the process is given in the appendix).

$$\frac{\hat{v}_{\mathrm{dc}i}}{\hat{v}_o} = \frac{f_{\mathrm{Ti}}G_{\mathrm{de2}}[v_{\mathrm{oref}}(1-2|D|)G_{\mathrm{PIo}} - D(1-|D|)]}{sC_1 + d_{\mathrm{d}}^*G_{\mathrm{is}}G_{\mathrm{PId}}G_{\mathrm{notch}}}$$
(42)

Based on (38) and (42), Bode plots of the transfer function $\hat{v}_{\mathrm{dc}i}/\hat{v}_o$ under the two control strategies are given in Fig. 8. The circuit parameters used for plot are listed in Table I. The control parameters of Control strategy I are the same as given in part D, section III. The controllers (G_{PId}, G_{PIo}) of Control strategy II can be calculated by (43), which is derived by letting its closed-loop transfer functions $\hat{v}_{\mathrm{dc}i}/\hat{v}_{\mathrm{dcref}}$, $\hat{v}_o/\hat{v}_{\mathrm{oref}}$ equal to that of Control strategy I. In such way the two strategies have the same control bandwidth for references' tracking. The balance controller G_{PIb} has the same gain as G_{PIo}.

$$\begin{cases} G_{\mathrm{PId}}d_{\mathrm{d}}^* = G_{\mathrm{d}}C_1 \\ G_{\mathrm{PIo}}v_{\mathrm{dcref}}NT_{\mathrm{hs}}n_{\mathrm{t}}(1-2|D|)/L_{\mathrm{t}} = G_oC_o \end{cases}$$
(43)

As shown in Fig. 8, the proposed control has much lower gain over the low-frequency range, indicating the minimized coupling between the dc-link and output voltage control loops.
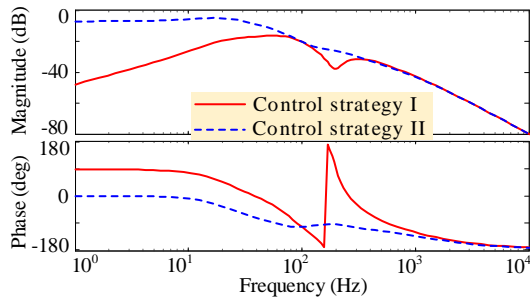

Fig.8 Comparison of Bode plots of the interference transfer function $\hat{v}_{\mathrm{dc}i}/\hat{v}_o$ under the two control strategies

B. Dc-Link Interaction and Output Impedance Analysis

In order to evaluate the dynamic performance and dc-link interaction in the case of load changes, the output impedances of the PET and CHB stage are derived and compared.

The PET output impedance Z_o can be derived as in (44) under Control strategy I, and as in (45) under Control strategy II,

according to the last row of the matrix equations (35) and (39), respectively:

$$Z_{o,\mathrm{I}} = \frac{\hat{v}_o}{\hat{i}_o} = \frac{G_{\mathrm{de2}} - 1}{sC_o + G_oC_oG_{\mathrm{de2}}}$$
(44)

$$Z_{o,\mathrm{II}} = \frac{\hat{v}_o}{\hat{i}_o} = \frac{-1}{sC_o + Nf_{\mathrm{Ti}}v_{\mathrm{dcref}}G_{\mathrm{de2}}(1-2|D|)G_{\mathrm{PIo}}}$$
(45)

The CHB stage output impedance Z_{dc} is an important factor in measuring the intermediate interaction and stability criterion of the cascaded systems [16]. Through derivation (given in the appendix)

$$Z_{\mathrm{dc,I}} = \frac{\hat{v}_{\mathrm{dc}i}}{\hat{i}_{1i}} = \frac{G_{\mathrm{is}}G_{\mathrm{notch}} - G_{\mathrm{de2}}}{G_{\mathrm{de2}}(sC_1 + G_{\mathrm{d}}C_1G_{\mathrm{is}}G_{\mathrm{notch}})}$$
(46)

$$Z_{\mathrm{dc,II}} = \frac{\hat{v}_{\mathrm{dc}i}}{\hat{i}_{1i}} = \frac{-1}{sC_1 + d_{\mathrm{d}}^*G_{\mathrm{PId}}G_{\mathrm{is}}G_{\mathrm{nocth}}}$$
(47)

The Bode plots of (44)-(47) are compared in Fig. 9. As can be observed, the output impedances of the CHB stage and the PET system are both reduced by the FEL control significantly. With lower output impedance, faster dynamic performance and better stability can be obtained in both the dc-link and output dc buses under load disturbance.
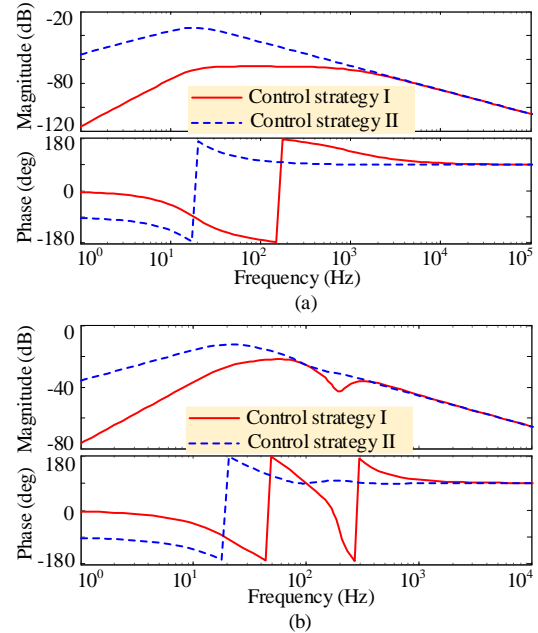

(a)

(b)

Fig.9 Comparison of output impedances of the CHB stage and the PET with different control strategies: (a) Bode diagram of $Z_{o\mathrm{I}}$ and $Z_{o\mathrm{II}}$ (b) Bode diagram of $Z_{\mathrm{dc,I}}$ and $Z_{\mathrm{dc,II}}$

V. SIMULATION AND EXPERIMENT VERIFICATION

A. Simulation Verification

In the simulations, a 3-module single-phase PET with 1.2MW rated power, which interconnects a 5.77kV ac grid (one phase of 10kV three-phase ac grid) and a 400V dc grid, is constructed to verify the proposed control strategy. The configuration of the PET model is based on Fig. 1, and the parameters are listed in Table I. The controller parameters are in line with those in part D, section III.

TABLE I SIMULATION PARAMETERS

Parameter	Value	Parameter	Value
v_s/ kV	5.77^{rms}	C_2/ mF	100
L_s/ mH	10	v_{oref}/ V	400
C_1/ mF	30	f_{CHB}/ kHz	2
v_{dcref}/ V	3000	f_{DAB}/ kHz	5
L_{t1}/ μH	360*0.8	N	3
L_{t2}/ μH	360	n_t	7.5:1
L_{t3}/ μH	360*1.2		

The dynamic performance of the cascaded PET with the proposed control is evaluated and compared with Control strategy II in the following simulations. The load power was abruptly changed from 1.2MW to -1.2MW at the time of 0.5s, and changed back to 1.2MW at 1s, and the grid voltage dropped by 20% at 1.5s. Note that in all the simulations and experiments, the reactive power maintained 0 var.

In Figure 10, the comparison of the dynamic responses of PET is made, including the output voltage v_o, the average value of the dc-link voltages v_{dcav}, the seven-level ac voltage of CHB v_{an}, grid voltage v_s and grid current i_s. As can be seen in Fig. 10, when the power reverses at 0.5s and 1s, the two dc-bus voltages, v_o and v_{dcav}, fluctuated with a magnitude less than 3V and 15V respectively under Control strategy I, significantly smaller than the fluctuations under Control strategy II (30V and 25V respectively). The faster recovering time of the dc bus voltages

and the faster dynamic response of the grid current can also be observed under Control strategy I.

Figure 11 shows the results of the three dc-link voltages of the sub modules. Under Control strategy I, minor fluctuations and better balancing performance of the dc-link voltages in the dynamic process can be observed in Fig. 11(a). While under Control strategy II, because of the coupling effect between the multi variables, the three dc-link voltages show different characteristics and great fluctuations in dynamic states when the circuit parameters are different. The maximum deviation between them is about 30V, and the recovering time is 0.1s, which both are much larger than those of Control strategy I.

Furthermore, Fig. 12 gives the compared results of the dc-link voltages when the power of the third module is disturbed. The disturbance is performed by connecting a 20 Ω resistance in parallel to the third module's dc-link during 0.50s to 0.51s. The dynamic deviations of the three dc-link voltages under the proposed control is much smaller than that under Control strategy II, although their average values v_{dcav} are almost identical. From the results of Figs. 11 and 12, much better decoupling performance of the proposed control can be observed.

In addition, from Figs. 10 and 11, at the time of 1.5s, we can see that both the two strategies have good ability in suppressing the grid voltage disturbance, since the same current controller with grid voltage feedforward was used.
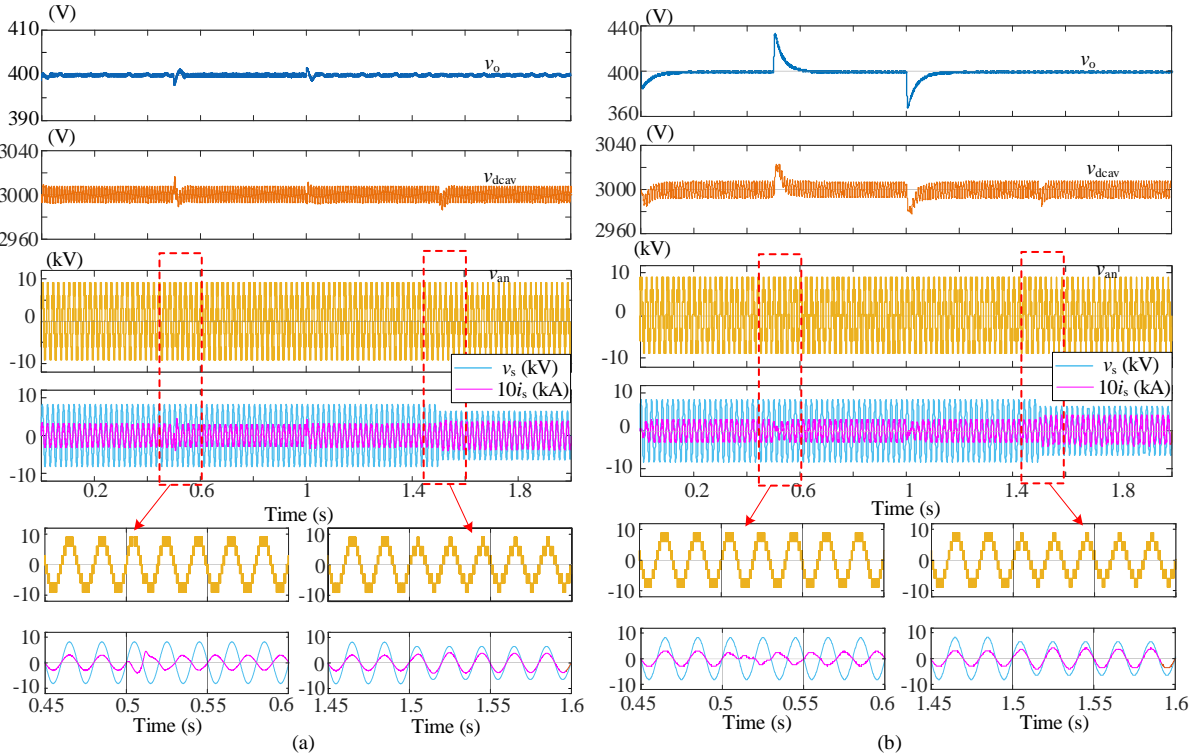

Fig.10 Dynamic response waveforms of the PET under the bidirectional load power changes and grid voltage drop, with (a) Control strategy I; (b) Control strategy II
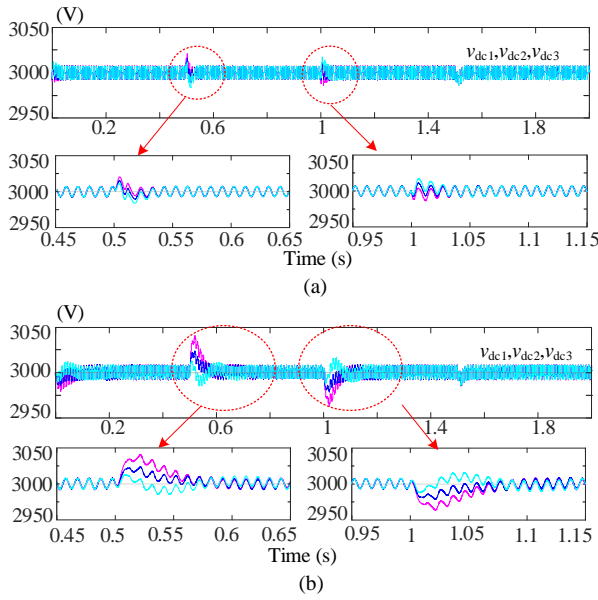
(a)

(b)

Fig.11 Dynamic waveforms of the three dc-link voltages under the bidirectional load power changes and grid voltage drop, with (a) Control strategy I; (b) Control strategy II
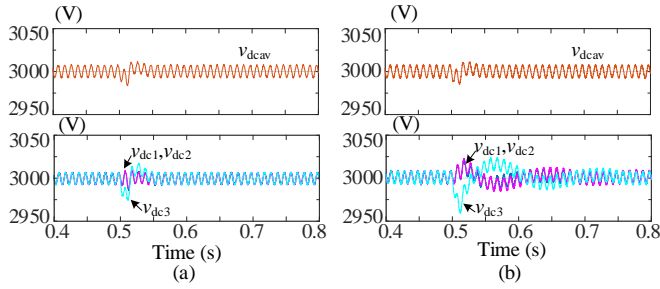

Fig.12 Dynamic waveforms of the dc-link voltages when the power of the third model disturbed, under (a) Control strategy I; (b) Control strategy II

B. Experimental Verification

The experiments of the cascaded PET were made on a scaled-down laboratory prototype consisting of one main controller unit (MCU), three HB rectifiers and three DAB modules, as shown in Fig.13. An active load is connected to the dc output of the PET, which is composed of a resister and a controlled dc voltage source, and can change from 1kW to -1kW. To implement the control algorithm, a DSP of TMS320F28335 is used in the MCU with 10kHz control frequency, and in MCU and the submodules, Xilinx FPGA chips are used for communication, sampling and pulse generation. The communications between the MCU FPGA and the submodule FPGAs are based on the optical fibers with a 2.5 Mb/s communicate rate, and the communication and sampling frequency is 20kHz. The parameters are given in Table II.
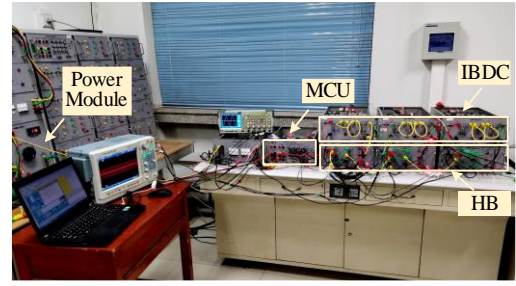

Fig.13 Experimental platform of cascaded PET

TABLE II   EXPERIMENTAL PARAMETERS

Parameter	Value	Parameter	Value
v_s/ V	180^{rms}	L_{t2}/ μH	128
L_s/ mH	10	L_{t3}/ μH	125
C_1/ mF	10	v_{oref}/ V	100
v_{dcref}/ V	100	f_{CHB}/ kHz	2
C_2/ mF	2.35	f_{DAB}/ kHz	5
n_t	1:1	N	3
L_{t1}/ μH	100		

In Figs. 14 and 15, the experiment results of the two control strategies are demonstrated respectively. In Fig. 14(a), under Control strategy I, when the load power reverses at t_1 and t_2, the maximum fluctuations of the output voltage and the dc-link voltages are 2V and 1V respectively, and their recovering time is about 0.25s. While under Control strategy II (Fig. 15(a)), the fluctuations of the output voltage and the dc-link voltages are 8V and 2.5V respectively, with recovering time of 0.5s. During the dynamic processes, better balancing performance of the three dc-link voltages were observed under the proposed control than under Control strategy II. So that the better decoupling effect and obviously improved dynamic responses in bidirectional power transitions can be verified.

The abrupt reversion of power can also be seen in the detail waveform of the grid current i_s in Fig. 14(b) and Fig. 15(b), which is in phase with grid voltage v_s when $t<t_1$ and out of phase with v_s when $t>t_1$. As can be seen, the grid current under the proposed control changes phase and enters the steady state faster.

Figure 14(c) and 15(c) give some experimental waveforms of the DAB converters under bidirectional power flow. v_{pri} and v_{sec} are the ac voltages on primary and secondary sides of the HF transformer, respectively. i_{L1} is the ac current of the storage inductance. In the positive power flow, the square wave voltage v_{pri} leads v_{sec} by a small phase as expected; while in reverse power, the results are opposite. In the dynamic intervals, the current response (i_{L1}) is faster under the proposed control.

From Figure 14(d) and 15(d), we can see that the input currents of each DAB modules are almost the same in steady states under both the two strategies, meaning that the DAB current sharing is automatically realized. And the better balancing performance of the currents can be observed under the proposed control.

Fig.14 Experimental results under Control strategy I (a) waveforms of v_o and v_{dci} (b) waveforms of v_s, i_s, and v_{an} (c) Waveforms of DAB variables, inductive ac current i_{L1}, and primary and secondary side ac voltages, v_{pri} and v_{sec} (d) Waveforms of input currents of each DAB module, i_{11}, i_{21}, i_{31}.
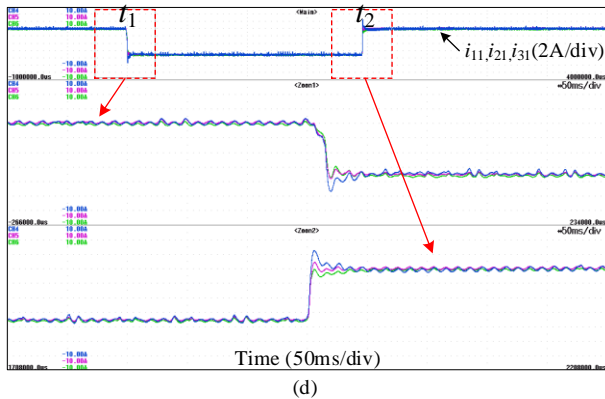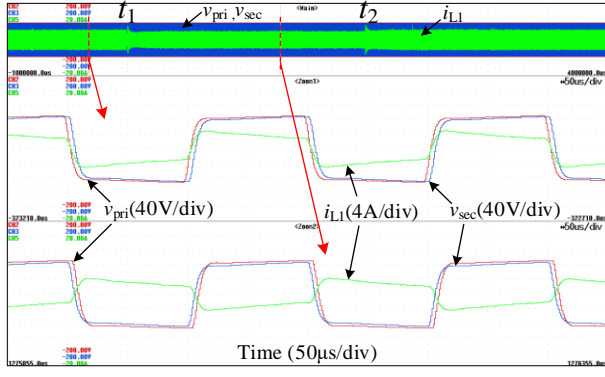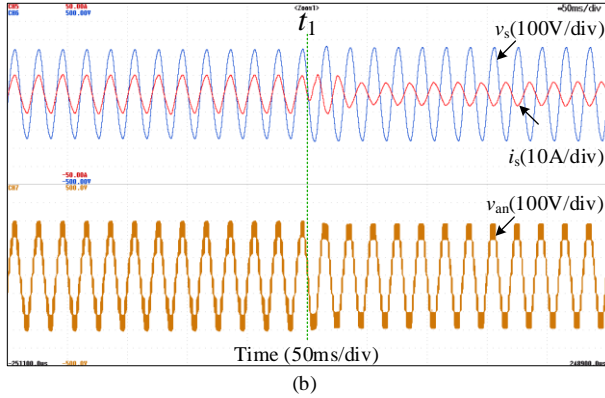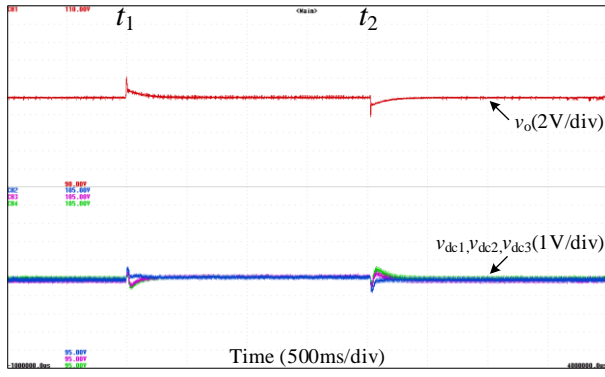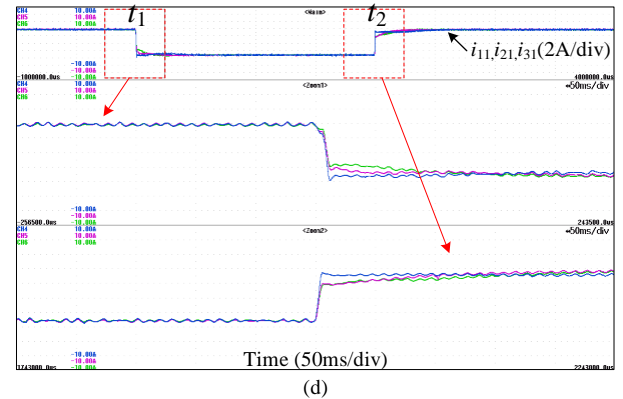
Fig.15 Experimental results under Control strategy II (a) waveforms of v_o and v_{dci} (b) waveforms of v_s, i_s, and v_{an} (c) Waveforms of DAB variables, inductive ac current i_{L1}, and primary and secondary side ac voltages, v_{pri} and v_{sec} (d) Waveforms of input currents of each DAB module, i_{11}, i_{21}, i_{31}.
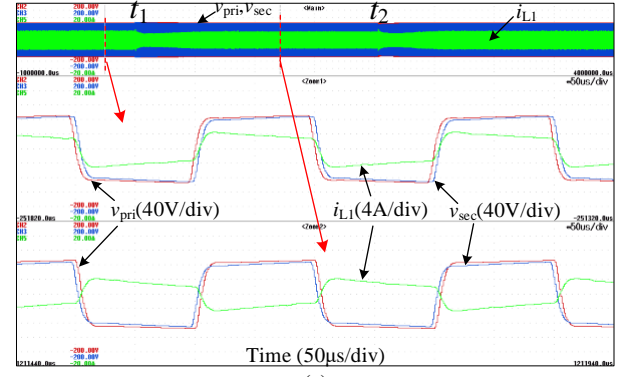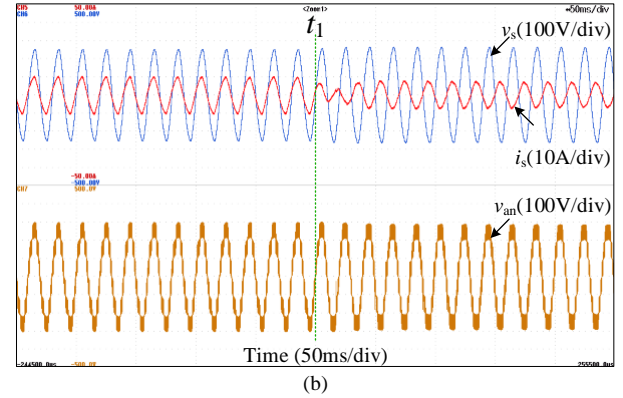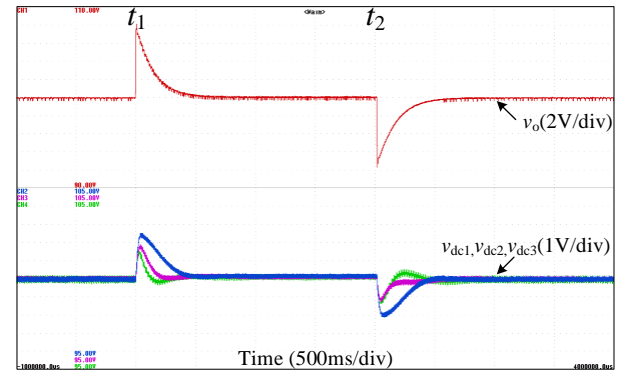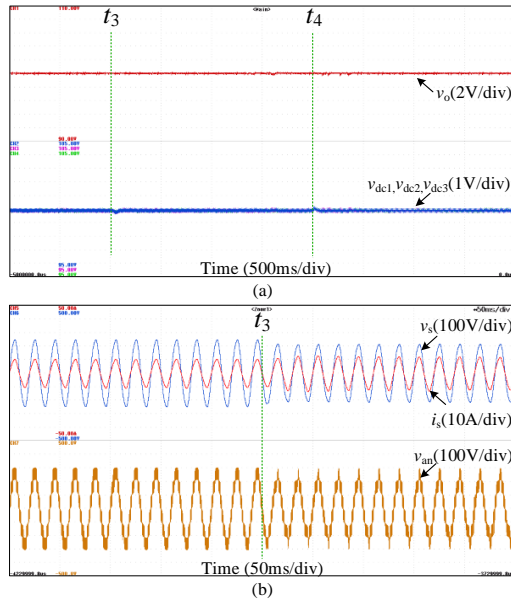
Fig.16 Experimental results of grid voltage disturbance under Control strategy I (a) waveforms of v_o and v_{dci} (b) waveforms of v_s, i_s, and v_{an}
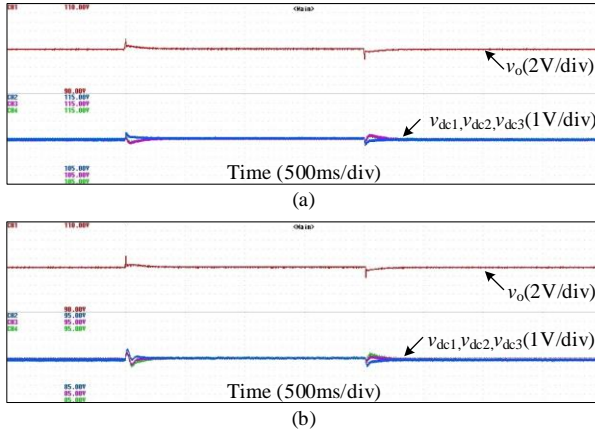

Fig.17 Experimental results with different DABs dc-voltage gains under Control strategy I (a) 100/110 (b) 100/90
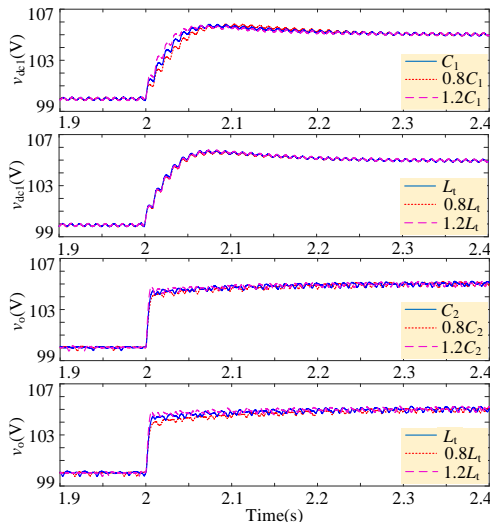

Fig.18 Responses for a set-point change under Control strategy I, with parametric uncertainty of $\pm 20\%$ on the capacitance and inductance values C_1, C_2, and L_t.

Figure 16 shows the experiment results when the grid voltage dropped by 12% at t_3 and recovered at t_4 under the proposed control. As is shown, the output and dc-link voltages are almost unaffected, and the grid current can rapidly enter the new steady state. Because the grid voltage feed-forward control is also used in Control strategy II, it has very similar waveforms as in Fig. 16 with the grid voltage changes, which is not repeated here for simplicity purpose.

Figure 17 shows the experiment results when the DABs dc voltage gains are not equal to 1. The load changes and the output voltage are as same as the experiment in Fig.14, but the dc-link voltage reference is set as 110V and 90V in Fig.17 (a) and (b), respectively. It can be found that there is almost no influence on the output voltage, and only a small difference on the dc link voltage, which means the proposed control strategy is robust to the dc voltage gains.

In Fig.18, the voltage responses are depicted for a set-point change with parametric uncertainty of $\pm 20\%$ on the capacitance and inductance values, C_1, C_2, and L_t, respectively. And the results indicate that the proposed control strategy is robust against the parametric uncertainties at steady states and during step changes.

VII. CONCLUSION

In this paper, a nonlinear decoupling control strategy based on the FEL technique is proposed for the modular cascaded PET. With the proposed strategy, the linearization and decoupling of all the control objectives can be realized, and the sub-module balances are naturally attained.

Combined with time-scale separation, the FEL control law of the current and voltage time-scales are derived separately, which can avoid the zero dynamics and simplify the nonlinear control design for the complex system. Then based on the linearized models of PET, a standardized design methodology for the controllers is realized to specify the desired control bandwidths and damping ratios of different control objectives, which means that it can provide an output features-tailored advantage for the PET in smart grid application.

Taken the dynamic influences of the current-loop, filter, and control delay into account, the further theoretical analyses of the decoupling effect and dynamic performance are made. The comparison analyses show that the proposed control has minimized coupling effect between the multi-control loops, reduced dc-link interaction, and also smaller output impedance of the PET. Under the conditions of bidirectional power changes and parameter inconsistency, the simulation and experimental results also proved that obviously improved dynamic responses and better sub-module balancing performance in dynamic process can be achieved.

In addition to the PET application, the proposed method may also be effective for the control of other combined complex power electronic systems to reduce coupling effect and achieve better dynamic performance. Considering the effects of transient state processes on the proposed control, such as the soft starting or grid fault, it's a very interesting topic and will be investigated in the future study. Moreover, the efficiency

optimization control integrated with the nonlinear control has not been considered in this paper, and will be developed in the subsequent research.

APPENDIX

In the following paper, the detailed deducing process of some equations in section IV is given.

A. Decoupling Effect between the Multi-Control Loops

1) The deducing process of equation (38)

Taking the *i*th ($i=1$-N) row of the state-space equation (35), and not considering the load current disturbance, the dynamic equation of $v_{\mathrm{d}ci}$ under Control strategy I can be written as:

$$s\hat{v}_{\mathrm{d}ci} = \frac{(G_{\mathrm{is}}G_{\mathrm{notch}} - G_{\mathrm{de}2})}{NC_1 v_{\mathrm{dcref}}}(Nf_{\mathrm{Ti}}Mv_{\mathrm{dcref}} - G_{\mathrm{o}}C_{\mathrm{o}}v_{\mathrm{oref}})\hat{v}_{\mathrm{o}} \\ -\frac{G_{\mathrm{d}}(G_{\mathrm{is}}G_{\mathrm{notch}} - G_{\mathrm{de}2})}{N}\sum_{i=1}^{N}\hat{v}_{\mathrm{d}ci} - G_{\mathrm{d}}G_{\mathrm{de}2}\hat{v}_{\mathrm{d}ci} \quad (A1)$$

Adding the first *N* rows of the state-space equation (35) up, leads to:

$$s\sum_{i=1}^{N}\hat{v}_{\mathrm{d}ci} = \frac{G_{\mathrm{is}}G_{\mathrm{notch}} - G_{\mathrm{de}2}}{C_1 v_{\mathrm{dcref}}}(Nf_{\mathrm{Ti}}Mv_{\mathrm{dcref}} - G_{\mathrm{o}}C_{\mathrm{o}}v_{\mathrm{oref}})\hat{v}_{\mathrm{o}} \\ -G_{\mathrm{d}}G_{\mathrm{is}}G_{\mathrm{notch}}\sum_{i=1}^{N}\hat{v}_{\mathrm{d}ci} \quad (A2)$$

Then substituting (A2) into (A1) to remove the term $\sum_{i=1}^{N}\hat{v}_{\mathrm{d}ci}$, yields equation (38) in section IV.

2) The deducing process of equations (39)-(41)

When using Control strategy II, as shown in Fig. 7(b), the phase shift ratio of DAB is composed of two parts, that is, $D_i = D - \Delta D_i$. D is the main phase shift ratio generated by the output voltage controller and ΔD_i is the additional term generated by the voltage balance controller.

Implementing small-signal perturbations to all the variables, i.e., $D_i = D + \hat{D} - \Delta\hat{D}_i$, $v_{\mathrm{d}ci} = v_{\mathrm{dcref}} + \hat{v}_{\mathrm{d}ci}$, $i'_{\mathrm{dref}} = I'_{\mathrm{dref}} + \hat{i}'_{\mathrm{dref}}$, and $v_{\mathrm{o}} = v_{\mathrm{oref}} + \hat{v}_{\mathrm{o}}$, $i_{\mathrm{o}} = I_{\mathrm{o}} + \hat{i}_{\mathrm{o}}$, the small signal form of the PET model (equation (33)) can be obtained as in (A3).

$$\begin{cases} sC_1\hat{v}_{\mathrm{d}ci} = d_{\mathrm{d}}^{*}G_{\mathrm{is}}\hat{i}'_{\mathrm{dref}} - f_{\mathrm{Ti}}G_{\mathrm{de}2}v_{\mathrm{oref}}(1-2|D|)(\hat{D}-\Delta\hat{D}_i) \\ \qquad - f_{\mathrm{Ti}}G_{\mathrm{de}2}D(1-|D|)\hat{v}_{\mathrm{o}} \\ \qquad\qquad\qquad\qquad\qquad\qquad\quad (i=1,\ldots,N) \\ sC_{\mathrm{o}}\hat{v}_{\mathrm{o}} = f_{\mathrm{Ti}}G_{\mathrm{de}2}[v_{\mathrm{dcref}}(1-2|D|)\sum(\hat{D}-\Delta\hat{D}_i) \\ \qquad + D(1-|D|)\sum\hat{v}_{\mathrm{d}ci}] - \hat{i}_{\mathrm{o}} \end{cases} \quad (A3)$$

where $d_{\mathrm{d}}^{*} = v_{\mathrm{d}}/(2Nv_{\mathrm{dcref}})$ is the steady state duty ratio of CHB.

From Fig. 7(b), the control variables under Control strategy II are calculated as:

$$\begin{cases} \hat{i}'_{\mathrm{dref}} = -G_{\mathrm{PId}}G_{\mathrm{notch}}\dfrac{\sum_{i=1}^{N}\hat{v}_{\mathrm{d}ci}}{N} \\ \hat{D} = -G_{\mathrm{PIo}}\hat{v}_{\mathrm{o}} \\ \Delta\hat{D}_{i(i=1\ldots N-1)} = (\dfrac{\sum_{i=1}^{N}\hat{v}_{\mathrm{d}ci}}{N} - \hat{v}_{\mathrm{d}ci})G_{\mathrm{PIb}} \\ \Delta\hat{D}_N = -\sum_{i=1}^{N-1}\Delta\hat{D}_i \end{cases} \quad (A4)$$

Substituting (A4) into (A3) yields (39)-(41).

3) The deducing process of equation (42)

Taking the *i*th ($i=1$-N) row of the state-space equation (39), the dynamic equation of $v_{\mathrm{d}ci}$ under Control strategy II can be written as:

$$s\hat{v}_{\mathrm{d}ci} = \frac{[f_{\mathrm{Ti}}G_{\mathrm{de}2}v_{\mathrm{oref}}(1-2|D|)G_{\mathrm{PIb}} - d_{\mathrm{d}}^{*}G_{\mathrm{is}}G_{\mathrm{PId}}G_{\mathrm{notch}}]\sum_{i=1}^{N}\hat{v}_{\mathrm{d}ci}}{NC_1} \\ -\frac{1}{C_1}f_{\mathrm{Ti}}G_{\mathrm{de}2}v_{\mathrm{oref}}(1-2|D|)\hat{v}_{\mathrm{d}ci}G_{\mathrm{PIb}} \\ +\frac{1}{C_1}f_{\mathrm{Ti}}G_{\mathrm{de}2}[v_{\mathrm{oref}}(1-2|D|)G_{\mathrm{PIo}} - D(1-|D|)]\hat{v}_{\mathrm{o}} \quad (A5)$$

Summing over *i* ($i=1$-N) to the equation (A5) leads to:

$$s\sum_{i=1}^{N}\hat{v}_{\mathrm{d}ci} = -\frac{1}{C_1}d_{\mathrm{d}}^{*}G_{\mathrm{is}}G_{\mathrm{PId}}G_{\mathrm{notch}}\sum_{i=1}^{N}\hat{v}_{\mathrm{d}ci} \\ +\frac{Nf_{\mathrm{Ti}}G_{\mathrm{de}2}}{C_1}[v_{\mathrm{oref}}(1-2|D|)G_{\mathrm{PIo}} - D(1-|D|)]\hat{v}_{\mathrm{o}} \quad (A6)$$

Substitute (A6) into (A5) to remove $\sum_{i=1}^{N}\hat{v}_{\mathrm{d}ci}$, then the equation (42) in section IV is obtained.

B. Dc-Link Interaction and Output Impedance Analysis

1) The deducing process of equation (46)

The output impedance of the CHB stage, Z_{dc}, equals to the transfer function of the dc-link voltage to the input current of the DAB, i_{1i}. According to equation (3), i_{1i} is rewritten as:

$$i_{1i} = f_{\mathrm{Ti}}v_{\mathrm{o}}G_{\mathrm{de}2}D_i(1-|D_i|) = f_{\mathrm{Ti}}v_{\mathrm{o}}G_{\mathrm{de}2}M_i \quad (B1)$$

Substituting (B1) into (33), the dynamic equation of $v_{\mathrm{d}ci}$ can be rewritten as:

$$sv_{\mathrm{d}ci} = -\frac{1}{C_1}i_{1i} + \frac{v_{\mathrm{d}}G_{\mathrm{is}}G_{\mathrm{notch}}i_{\mathrm{dref}}}{2C_1\sum_{i=1}^{N}v_{\mathrm{d}ci}} \quad (B2)$$

According to (20), M_i is expressed as:

$$M_i = k_{\mathrm{A}}v_i + k_{\mathrm{B}}i_{\mathrm{dref}} \\ = \frac{v_{\mathrm{d}}}{2\sum v_{\mathrm{d}ci}f_{\mathrm{Ti}}v_{\mathrm{o}}}i_{\mathrm{dref}} - \frac{C_1}{f_{\mathrm{Ti}}v_{\mathrm{o}}}G_{\mathrm{d}}(v_{\mathrm{dcref}} - v_{\mathrm{d}ci}) \quad (B3)$$

From (B1) and (B3), then

$$i_{1i} = G_{\mathrm{de}2}[\frac{v_{\mathrm{d}}}{2\sum v_{\mathrm{d}ci}}i_{\mathrm{dref}} - C_1 G_{\mathrm{d}}(v_{\mathrm{dcref}} - v_{\mathrm{d}ci})] \quad (B4)$$

From (B2) and (B4), i_{dref} is eliminated, and then the output impedance of CHB stage under Control strategy I (equation (46)) is obtained.

2) The deducing process of equation (47)

From (4) and (A3), the dynamic equation of $v_{\mathrm{d}ci}$ can be written as:

$$sC_1\hat{v}_{\mathrm{d}ci} = d_{\mathrm{d}}^{*}G_{\mathrm{is}}\hat{i}'_{\mathrm{dref}} - \hat{i}_{1i} \quad (B5)$$

When ignoring the dc-link voltage imbalance of each module, $\hat{i}'_{\mathrm{dref}}$ in (A4) can be rewritten as:

$$\hat{i}'_{\mathrm{dref}} = -G_{\mathrm{PId}}G_{\mathrm{notch}}\hat{v}_{\mathrm{d}ci} \quad (B6)$$

Substituting (B6) into (B5), the output impedance of the equation (47) can be obtained.

REFERENCES

[1] M. Liserre, G. Buticchi, M. Andresen and et al, "The smart transformer: Impact on the electric grid and technology challenges," *IEEE Ind. Electron. Mag.*, vol. 10, no. 2, pp. 46–58, Jun. 2016

[2] L. F. Costa, G. D. Carne, G. Buticchi and et al, "The smart transformer: A solid-state transformer tailored to provide ancillary services to the distribution grid," *IEEE Power Electronics Magazine*, vol. 4, no. 2, pp. 56-67, Jun. 2017.

[3] A. Q. Huang, M. L. Crow, G. T. Heydt and et al, "The future renewable electric energy delivery and management (FREEDM) system: the energy internet," *Proceedings of the IEEE*, vol. 99, no.1, pp. 133-148, Jan. 2011.

[4] X. She, A. Q. Huang, and R. Burgos, "Review of solid-state transformer technologies and their application in power distribution systems," *IEEE Journal of Emerging and selected topics in power electronics*," vol. 1, no.3, pp. 186-198, Sep. 2013.

[5] J. Tian, C. Mao, D. Wang and et al, "A short-time transition and cost saving redundancy scheme for medium-voltage three-phase cascaded H-bridge Electronic power transformer," *IEEE Trans. Power Electron.*, vol. 33, no. 11, pp. 9242-9252, Nov. 2018.

[6] J. Shi, W. Gou, H. Yuan and et al, "Research on voltage and power balance control for cascaded modular solid-state transformer," *IEEE Trans. Power Electron.*, vol. 26, no. 4, pp. 1154-1166, April 2011.

[7] X. She. "Control and design of a high voltage solid state transformer and its integration with renewable energy resources and microgrid system," Ph. D. dissertation, North Carolina State University, Raleigh, North Carolina, 2013.

[8] T. Zhao, G. Wang, S. Bhattacharya et al., "Voltage and power balance control for a cascaded H-bridge converter based solid-state transformer," *IEEE Trans. Power Electron.*, vol. 28, no. 4, pp. 1523-1532, Apr. 2013.

[9] X. She, A. Q. Huang, and X. Ni, "Current sensorless power balance strategy for DC/DC converters in a cascaded multilevel converter based solid state transformer," *IEEE Trans. Power Electron.*, vol. 29, no. 1, pp. 17-22, Jan. 2014.

[10] J. Liu, J. Yang, J. Zhang and et al, "Voltage balance control based on dual active bridge DC/DC converters in a power electronic traction transformer," *IEEE Trans. Power Electron.*, vol. 33, no. 2, pp. 1696-1714, Feb. 2018.

[11] G. Wang, X. She, F. Wang and et al, "Comparisons of different control strategies for 20kVA solid state transformer," *2011 IEEE Energy Conversion Congress and Exposition*, Phoenix, AZ, 2011, pp. 3173-3178.

[12] X. She, A. Q. Huang, T. Zhao and et al, "Coupling effect reduction of a voltage-balancing controller in single-phase cascaded multilevel converters," *IEEE Trans. Power Electron.*, vol. 27, no. 8, pp. 3530-3543, Aug. 2012.

[13] J. Ge, Z. Zhao, L. Yuan, T. Lu and et al, "Energy feed-forward and direct feed-forward control for solid-state transformer," *IEEE Trans. Power Electron.*, vol. 30, no. 8, pp. 4042-4047, Aug. 2015.

[14] A. Riccobono and E. Santi, "Positive feedforward control of three-phase voltage source inverter for dc input bus stabilization with experimental validation," *IEEE Trans. Ind. Appl.*, vol. 49, no. 1, pp. 168-177, Jan.-Feb. 2013.

[15] Y. Tian, Z. Chen, F. Deng and et al, "Active power and DC voltage coordinative control for cascaded DC-AC converter with bidirectional power application," *IEEE Trans. Power Electron.*, vol. 30, no. 10, pp. 5911-5925, Oct. 2015.

[16] Y. Tian, P. C. Loh, F. Deng and et al, "Impedance coordinative control for cascaded converter in bidirectional application," *IEEE Trans. on Ind. Appl.*, vol. 52, no. 5, pp. 4084-4095, Sept.-Oct. 2016.

[17] H. Liu, C. Mao, J, Lu and et al, "Optimal regulator-based control of electronic power transformer for distribution systems," Electric Power Systems Research, vol. 79, no. 6, pp. 863-870, Jun. 2009.

[18] H. Beiranvand and E. Rokrok, "Asymptotically stable controller for SSTs based on Lyapunov direct stability method," *IET Power Electronics*, vol. 10, no. 15, pp. 2065-2075, Dec, 2017.

[19] L. Tarisciotti, P. Zanchetta, A. Watson and et al, "Multi objective modulated model predictive control for a multilevel solid-state transformer," *IEEE Trans. Ind. Appl*, vol. 51, no. 5, pp. 4051-4060, Sept.-Oct. 2015.

[20] R. Hooshmand, M. Ataei, M. Rezaei, "Improving the dynamic performance of distribution electronic power transformers using sliding mode control," *Journal of Power Electronics*, vol. 12, no. 1, pp. 145-156, Jan. 2012.

[21] H. Liu, J. Yang, C. Mao and et al, "Nonlinear control of electronic power transformer for distribution system using feedback linearization," in *2011 IEEE Power Engineering and Automation Conference*, Wuhan, China, 2011, pp. 22-26.

[22] M. Salimi and S. Siami, "Closed-loop control of dc-dc buck converters based on exact feedback linearization," in *2015 4th International Conference on Electric Power and Energy Conversion Systems (EPECS)*, Sharjah, 2015, pp. 1-4.

[23] D. Lee, G. Lee, K. Lee, "DC-bus voltage control of three-phase ac/dc PWM converters using feedback linearization," *IEEE Trans. Ind. Appl.*, vol. 36, no. 3, pp. 826-833, May-June 2000.

[24] T.-S. Lee. "Input-output linearization and zero-dynamics control of three-phase ac/dc voltage-source converters," *IEEE Trans. Power Electron.*, vol. 18, no. 1, pp. 11-22, Jan. 2003.

[25] X. Lai, J. Le. "A novel nonlinear control strategy for single-phase APF based on feedback linearization," in *2011 International Conference on Electrical and Control Engineering*, Yichang, China, 2011, pp. 3305-3308.

[26] D. R. Espinoza-Trejo, E. Bárcenas-Bárcenas, D. U. Campos-Deelgado and et al, "Voltage-oriented input-output linearization controller as maximum power point tracking technique for photovoltaic systems," *IEEE Trans. Ind. Electron.*, vol. 62, no. 6, pp.3499-3507, Jun. 2015.

[27] S. Yang, P. Wang and Y. Tang. "Feedback linearization-based current control strategy for modular multilevel converters," *IEEE Trans. Power Electron.*, vol. 33, no. 1, pp. 161-174, Jan. 2018.

[28] Y. Sun, J. Liu and C. Fu, "Nonlinear PR control strategy for cascaded H-bridge rectifier based on state feedback linearization," in *2017 20th International Conference on Electrical Machines and Systems (ICEMS)*, Sydney, NSW, AUS, 2017, pp.1-6.

[29] H. Beiranvand, E. Rokrok, H. Acikgoz, M. Liserre, "Two-stage Input-Output Feedback linearization controller for AC-AC converter-based SST," in *2019 10th International Power Electronics, Drive Systems and Technologies Conference (PEDSTC)*, Shiraz, Iran, 2019, pp. 343-348.

[30] B. Bahrani, A. Rufer, S. Kenzelmann and L. A. C. Lopes, "Vector control of single-phase voltage-source converters based on fictive-axis emulation," *IEEE Trans. Ind. Appl.*, vol. 47, no. 2, pp. 831-840, March-April 2011.

[31] Alberto Isidori, Nonlinear control systems, 3rd ed., London, UK: Springer-Verlag, 1995, pp. 219–277.

Yuwei Sun received the M.S. and Ph.D. degrees in electrical engineering from the North China Electric Power University, Baoding and Beijing, China, in 2013 and 2018, respectively.

She is currently a Lecturer with the Department of Electric Power Engineering, North China Electric Power University, Baoding, China. Her current research interests include power electronics technology applications in power system and key technology of power electronic transformer.
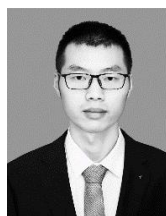
Jilin Zhu received his B.S degree in electrical engineering and automation from North China Electric Power University, Baoding, China, in 2018. He is currently working towards the M.S degree at North China Electric Power University.

His research interests include the modeling and control strategy of power electronic transformer.

Chao Fu received the M.S. and Ph.D. degrees in electrical engineering from the North China Electric Power University, Baoding and Beijing, China, in 2006 and 2012, respectively.

He is currently a Lecturer with Department of Electric Power Engineering, North China Electric Power University, Baoding, China. His current research interests include renewable energy generation and power electronics technology applications in power systems.

Zhe Chen (M'95–SM'98–F'19) received the B.Eng. and M.Sc. degrees all in Electrical Engineering from Northeast China Institute of Electric Power Engineering, Jilin City, China, MPhil in Power Electronic, from Staffordshire University, England and the Ph.D. degree in Power and Control, from University of Durham, England.

Dr Chen has been a full Professor with the Department of Energy Technology, Aalborg University, Denmark since 2002. He is the leader of Wind Power System Research program at the Department of Energy Technology, Aalborg University and the Danish Principle Investigator for *Wind Energy* of *Sino-Danish Centre for Education and Research*. His main current research interests are power electronics, power grids and new energy technologies. He has led and participated in many research and industrial projects and has been a panel member of research funding evaluation committees in many EU countries.

Dr Chen is an Associate Editor of the IEEE Transactions on Power Electronics, a member of editorial boards for many international journals, a Fellow of the Institution of Engineering and Technology (London, U.K.), and a Chartered Engineer in the U.K.